Available online at www.sciencedirect.com

ScienceDirect

Acta Materialia 61 (2013) 7582–7590

Acta MATERIALIA

www.elsevier.com/locate/actamat

Atomic-scale investigation of ε and θ precipitates in bainite in 100Cr6 bearing steel by atom probe tomography and ab initio calculations

W. Song [a], J. von Appen [b], P. Choi [c], R. Dronskowski [b], D. Raabe [c], W. Bleck [a,*]

[a] Department of Ferrous Metallurgy, RWTH Aachen University, Aachen, Germany
[b] Institute of Inorganic Chemistry, RWTH Aachen University, Aachen, Germany
[c] Department of Microstructure Physics and Alloy Design, Max-Planck-Institut für Eisenforschung, Düsseldorf, Germany

Received 14 March 2013; received in revised form 20 August 2013; accepted 25 August 2013
Available online 3 October 2013

Abstract

Carbide precipitation during upper and lower bainite formation in high-carbon bearing steel 100Cr6 is characterized using transmission electron microscopy and atom probe tomography. The results reveal that both ε and θ carbides precipitate in lower bainite isothermally held at 260 °C and only θ precipitates form in upper bainite isothermally held at 500 °C. ε and θ precipitate under paraequilibrium condition at 260 °C in lower bainite and θ precipitates under negligible partitioning local equilibrium condition in upper bainite at 500 °C. In order to theoretically study ε and θ precipitation and the ε → θ transition in bainite, thermodynamic calculations have been carried out using ab initio techniques. We find that ε and θ carbides in ferrite have almost identical thermodynamic stability, and hence have similar formation probability. In austenite, however, cementite formation is clearly preferred: it is favored by 5 kJ mol^{-1} at room temperature and still by 4 kJ mol^{-1} at 500 °C. Hence, the thermodynamic predictions agree well with the atom probe tomography results.

Keywords: ε carbide; Cementite; Atom probe tomography; Ab initio

---

1. Introduction

100Cr6 with the nominal composition of 1 wt.% C–0.3 wt.% Si–0.3 wt.% Mn–1.5 wt.% Cr is a high-carbon steel, which is widely used in automotive and bearing applications. In order to achieve high strength, high wear resistance and good fatigue properties, it is rendered into either a martensitic and/or bainitic state. Nanosized carbides precipitated from martensite and/or bainite play a very important role in determining the mechanical properties of the material. Barrow et al. [1] showed that maximum strength and hardness can be achieved with high carbon concentrations and fine ε carbides in an early stage of precipitation, though this results in the material having limited ductility. Furthermore, Barrow et al. [1] and Kang et al. [2] recently reported that the precipitate microstructure in 100Cr6 not only determines its static mechanical properties (hardness, strength and ductility), but also its dynamic response during rolling contact fatigue. Precipitate shearing, particle dissolution, dislocation cell and nanocrystal formation as well as matrix/carbide debonding are features commonly observed throughout bearing life. Typically, these microstructural changes are initiated at a scale of only a few nanometers, yet can cause cracks that grow up to several millimeters during ongoing loading [2]. ε carbide precipitation during tempering of quenched martensite has been intensively investigated [3–14]; however, its precipitation from a bainitic matrix has not yet been well understood. Lai [15] observed, by transmission electron microscopy (TEM), ε carbides with the same orientation relationship of $\langle 1 1 0\rangle_\alpha \parallel \langle 1 1 \bar{2} 0\rangle_\varepsilon$ in both lower bainite and tempered martensite. This observation would support the view that ε carbides precipitate directly from supersaturated ferrite

---

[*] Corresponding author. Tel.: +49 241 80 95782.
E-mail address: wolfgang.bleck@iehk.rwth-aachen.de (W. Bleck).

1359-6454/$36.00 © 2013 Acta Materialia Inc. Published by Elsevier Ltd. All rights reserved.
http://dx.doi.org/10.1016/j.actamat.2013.08.051

in lower bainite. Caballero et al. [16] recently studied a high-carbon (0.98 wt.%) high-silicon (1.46 wt.%) steel. Using atom probe tomography (APT), they detected ε carbide in bainite tempered at 400 °C and observed an $\varepsilon \rightarrow \theta$ transition in bainite tempered at 500 °C.

θ carbide (cementite Fe_3C) is orthorhombic with a carbon content of 25 at.%. Hexagonal ε carbides are described as ε-$Fe_{2.x}C$ with a carbon content between ε-Fe_3C and ε-Fe_2C. For the carbon-richer version of this carbide, however, both, composition and crystallographic structure have been a matter of debate since the 1940s when the first syntheses of ε-Fe_2C were reported [17]. It was Jack [18] who questioned this composition and proposed instead a partially ordered $Fe_{20}C_9$ (=$Fe_{2.22}C$) composition as the upper limit of the carbon solubility. Until now, there are authors claiming the existence of ε-Fe_2C [19,20] as well as other authors who question its existence [21]. Other sources report carbides that have slightly varying carbon contents ($Fe_{2.2}C$–$Fe_{2.4}C$), namely between both stoichiometric phases ε-Fe_3C and ε-Fe_2C [22,23]. The ε carbide discussed here is ε-$Fe_{2.4}C$ with a theoretical carbon content of ~29.4 at.%. The lattice parameters of this ε carbide are $a_h = 2.752$ Å and $c_h = 4.353$ Å [3].

In the present work, we study ε and θ carbide precipitation and elemental partitioning features associated with ε and θ precipitation in both upper and lower bainite formation, in high-carbon bearing steel 100Cr6 using TEM and APT. Ab initio (density-functional) predictions together with quasi-harmonic phonon calculations were further performed in order to assess the thermodynamics associated with ε carbide ($Fe_{2.4}C$) formation and its competition with θ carbide (cementite Fe_3C) precipitation. The possibility of the existence of ε carbide and the arrangement of the carbon atoms in hexagonal ε carbide are further discussed in terms of thermodynamic simulations.

2. Experimental methods and material processing

The chemical composition of the steel 100Cr6 is given in Table 1. The material is mainly alloyed with Cr and microalloyed with Mo. Si and Mn are both at a low level, while the Al content is almost negligible. The N content in the steel is 75 ppm.

After hot forging, the material was soft annealed at 800 °C followed by a subsequent slow cooling to room temperature. After soft annealing, the microstructure was characterized by a homogeneous distribution of fine, spheroidized carbides in a ferritic matrix. Samples were subsequently heated up at a rate of 3.3 °C s^{-1} and austenitized at 850 °C for 300 s, followed by rapid cooling to 260 and 500 °C at a rate of 55 °C s^{-1}. At the isothermal transformation temperature (ITT) of 260 °C, the samples were isothermally held for 2500 s in order to form a lower bainite microstructure. At the ITT of 500 °C the samples were isothermally held for 1200 s in order to form an upper bainite microstructure. The heat-treatment cycles are illustrated in Fig. 1. Austenitization and bainitization were performed in a Bähr 805A dilatometer, using specimens 3 mm in diameter and 10 mm long.

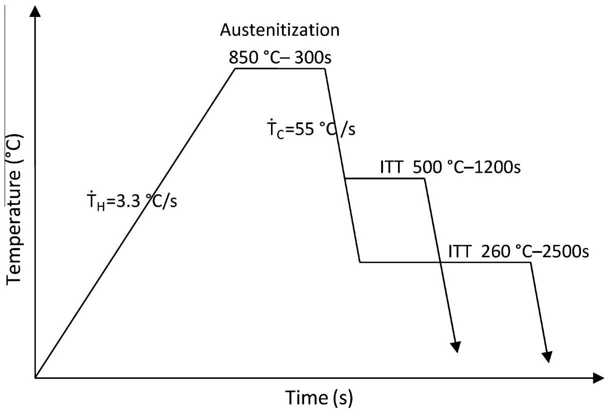

Fig. 1. Heat treatment cycle of the investigated steel 100Cr6 (ITT stands for Isothermal Transformation Temperature).

To characterize the bainitic morphology, a Tecnai F20G2 transmission electron microscope with an embedded US1000 Gatan camera was used. TEM foils were prepared from the heat-treated specimen with a twin-jet electropolishing device, using a chemical solution of 10 vol.% perchloric acid and 90 vol.% acetic acid. APT specimens were cut from the heat-treated material and electropolished with standard electropolishing methods [24]. APT analyses were performed using a Local Electrode Atom Probe (LEAP 3000X HR, Cameca Instruments) in pulsed voltage mode at a pulse fraction of 15% and a pulse frequency of 200 kHz. The specimen base temperature was about 60 K [25–28].

3. Simulation methods

All first-principles electronic-structure calculations were based on density-functional theory [29,30]. The simulations were performed by using the augmented (PAW [31]) plane-wave approach using the Vienna Ab initio Simulation Package [32–34]. Structural optimizations were carried out in terms of volume, cell shape and ionic positions. In the next step, the lattice vectors were scaled from 91% to 104% of those of the equilibrium structure, and optimizations of both the cell shape and the ionic positions were performed using fixed volumes. Phonon properties were

Table 1
Chemical composition of the investigated steel 100Cr6 (wt.%).

Fe	C	Si	Mn	P	S	Cr	Mo	Ni	Al	Cu	N
Bal.	0.967	0.30	0.23	0.003	<0.001	1.38	0.02	0.07	0.026	0.05	0.0075

computed by the direct force constant method [35] as implemented in the FROPHO code [36,37]. To avoid self-interactions while calculating the Hellmann–Feynman forces [38,39], supercells were used with lattice parameters >10 Å. Volume expansions and temperature-dependent thermodynamic properties were evaluated in the framework of the quasi-harmonic approximation [40,41], taking into account the electronic ground state and the harmonic vibrational contributions to the Helmholtz free energy for various volumes. The vibrational free energy was fitted as a linear function of the volume in order to reduce calculation time.

4. Results and discussion

4.1. Morphology

Fig. 2 shows TEM micrographs of bainite microstructures in the investigated steel 100Cr6. Lower bainite and upper bainite in 100Cr6 exhibit distinct morphological features. The bright-field TEM image in Fig. 2a shows lower bainite microstructure in the sample isothermally heat-treated at 260 °C for 2500 s. As shown in Fig. 2a, nanosized carbides precipitate within bainitic ferrite α_B plates and the particles precipitate with an angle of ~60° to the longitudinal direction of bainitic ferrite α_B. The boundaries of the bainitic ferrite α_B subunits are indicated in Fig. 2a in terms of dashed lines.

The bright-field TEM image in Fig. 2b shows the upper bainite microstructure in the sample isothermally heat-treated at 500 °C for 1200 s. Unlike the plate-like morphology of bainitic ferrite α_B observed in lower bainite it adopts a more lath-type shape in upper bainite. As shown in Fig. 2b, nanosized carbides are precipitated between the bainitic ferrite laths in the upper bainite. Several carbides precipitate from the grain boundary (GB) shown at the right bottom of Fig. 2b. The carbides found in the upper bainite are much longer and thicker than the carbides in the lower bainite. Some of these precipitates have already merged to a larger carbide particle. The TEM images reveal that the average size of nanosized carbides in lower bainite is about 30 nm in width and about 80 nm in length, while in upper bainite, the coarsened carbides are even as large as 100 nm in width and 0.5–1 μm in length.

4.2. Atom probe tomography

The 3-D carbon atom map of the sample isothermally heat-treated at 260 °C for 2500 s is shown in Fig. 3a. It provides a local overview of the carbon distribution in bainitic ferrite α_B matrix and carbides. As shown in Fig. 3a, the distribution of the carbon atoms in the analysis volume is not uniform. The carbon-depleted region with a carbon content of <1.2 at.% represents the bainitic ferrite α_B, which is supersaturated with carbon [25]. The carbon-rich regions correspond to θ carbide (cementite Fe_3C) and ε carbide $Fe_{2.4}C$. We identify the particle with a carbon content of ~25 at.% as cementite (θ) and the particle with a carbon content of ~29.4 at.% as ε carbide $Fe_{2.4}C$, both owing to their respective stoichiometries. To further analyze these two particles, two regions of interest (ROI) were selected. On the other hand, the distribution of the carbon atoms within the bainitic ferrite α_B matrix is not uniform either. The carbon content ranges from 0.3 to 1.2 at.%. The carbon atom map in Fig. 3a shows small regions of carbon agglomeration which might be caused by carbon concentration perturbation in the bainitic ferrite α_B matrix, such as possibly caused by carbon-enriched internal interfaces.

In order to precisely analyze the compositional distribution of carbon and the other alloying elements in the particles, more detailed mass spectrum analyses of ROI1 and ROI2 in Fig. 3a were separately carried out on these specific subvolumes. The chemical compositions in the particles observed in ROI 1 and ROI 2 are listed in Table 2. Spectrum peaks with a mass-to-charge ratio of 24 Da can be either assigned to C_2^+ or C_4^{++} ions [42,43]. Using the mass-to-charge ratio of 24.5 Da, which can be unambiguously assigned to C_4^{++} ions, namely $(C_3^{12}C^{13})^{++}$, we applied a peak devolution algorithm for the mass-to-charge peak 24 Da. We found that C_4^{++} ions make up 90 % of the peak at 24 Da and hence assigned this peak to C_4^{++} for plotting the 1-D concentration profiles. This procedure leads to a slight overestimation of the carbon concentration inside the particles, as determined from the 1-D concentration profiles.

Fig. 3b and c display 1-D concentration profiles (fixed sample count profiles, using a bin size of 5000 atoms) of carbon and alloying elements in nanosized carbides and the adjacent bainitic ferrite α_B matrix region in lower bainite in the investigated material 100Cr6 isothermally heat-treated at 260 °C for 2500 s. The 1-D concentration profile of the carbon-enriched particle in ROI1 is plotted in Fig. 3b, showing the compositions of carbon and alloying elements in bainitic ferrite matrix α_B and cementite (θ) with a carbon concentration of ~25 at.%. The substitutional elements are distributed with the same compositions in both bainitic ferrite and cementite (θ). More specifically, the concentration profile indicates no significant enrichment of substitutional elements at the interface between bainitic ferrite and cementite (θ). In addition, the 1-D concentration profile of the carbon-enriched particle observed in ROI2 is plotted in Fig. 3c, showing the compositions of carbon and the other alloying elements in the bainitic ferrite α_B matrix and also in the ε carbide $Fe_{2.4}C$ with a carbon concentration of ~29.4 at.%. The data reveal that the substitutional elements are distributed homogeneously in both bainitic ferrite and ε carbide $Fe_{2.4}C$. The carbon atoms are near-equilibrated and there is no partitioning of any substitutional elements between the bainitic ferrite α_B and the ε carbide $Fe_{2.4}C$. Therefore, we conclude that both cementite (θ) and ε carbide $Fe_{2.4}C$ precipitate without partitioning of substitutional elements in lower bainite in the investigated material 100Cr6 when isothermally heat-treated at 260 °C for 2500 s. The features of substitutional

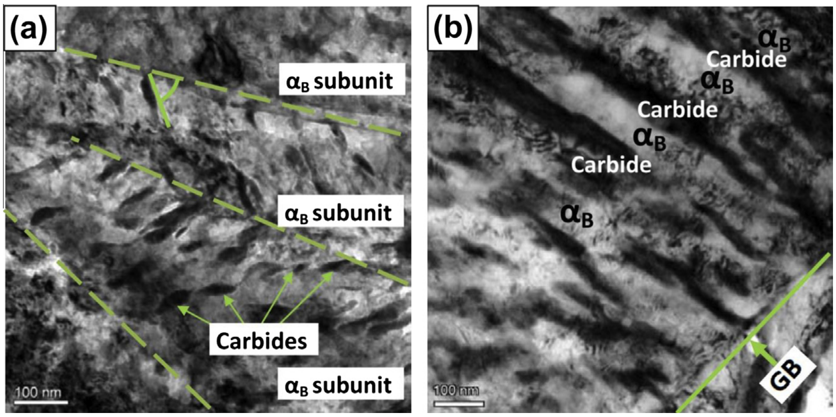

Fig. 2. TEM micrographs of 100Cr6 steel: (a) lower bainite at 260 °C for 2500 s, (b) upper bainite at 500 °C for 1200 s; α_B: bainitic ferrite, θ: cementite, GB: grain boundary.

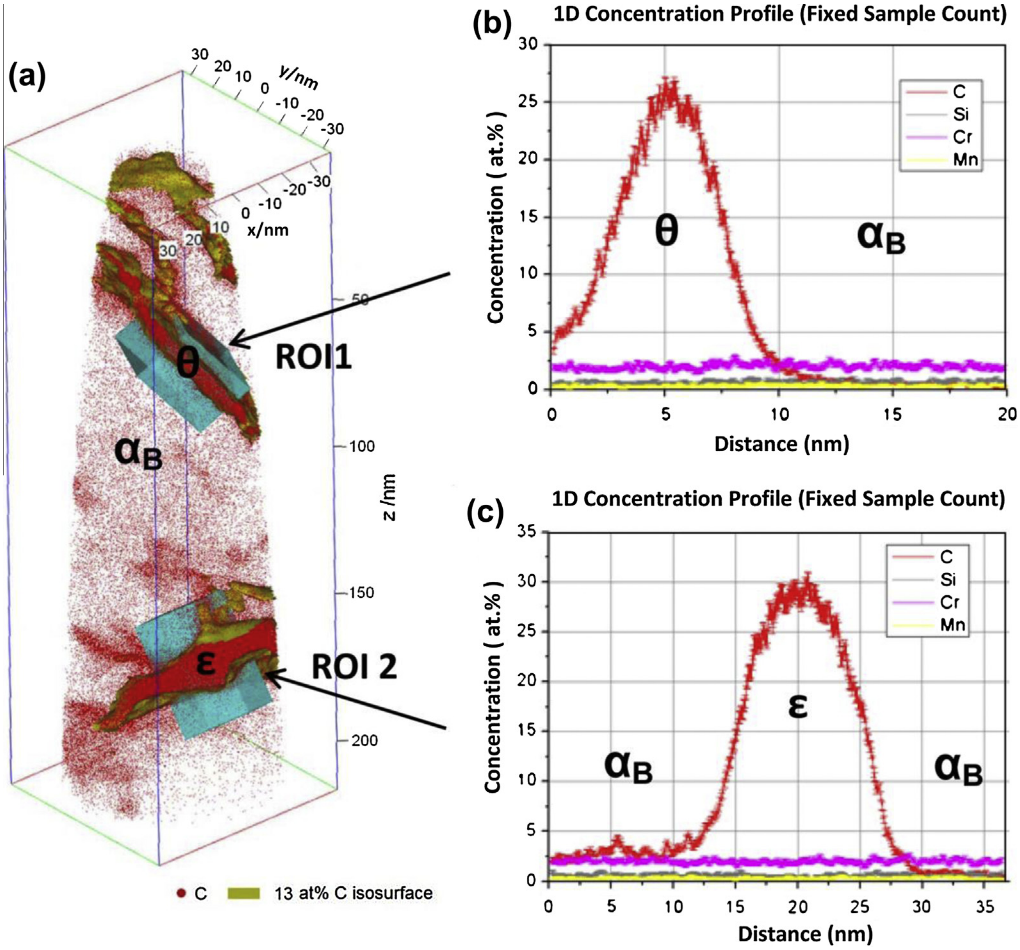

Fig. 3. (a) Carbon atomic map and 13 at.% iso-concentration surface in lower bainite in 100Cr6 isothermally heat-treated at 260 °C for 2500 s; ID concentration profile in ROI1 (b) and ROI2 (c) in Fig. 3(a); α_B: bainitic ferrite, θ: cementite, ε: ε carbide $Fe_{2.4}C$.

Table 2
Chemical compositions in the particles in ROI1 and in ROI2.

Element	C	Si	Mn	Cr	Ni	Al	Cu
ROI1 (at.%)	25.58	0.474	0.298	1.879	0.065	0.028	0.042
ROI2 (at.%)	30.79	0.521	0.293	1.836	0.049	0.034	0.032

element distribution across the bainitic ferrite α_B/cementite (θ) interface and the bainitic ferrite α_B/ε carbide $Fe_{2.4}C$ interface hence imply that both cementite (θ) and ε carbide $Fe_{2.4}C$ precipitation in lower bainite occur under paraequilibrium mode [44,45]. “Paraequilibrium mode” refers to the phase transformation mode which assumes that only interstitial alloy elements, e.g. C, N, redistribute by long-range diffusion, whereas substitutional alloy elements, e.g. Cr, Mn, Si, are considered to be frozen in the sublattice.

Both cementite (θ) and ε carbide $Fe_{2.4}C$ in lower bainite isothermally heat-treated at 260 °C for 2500 s were repeatedly observed in the current APT measurements. The particles which were detected in this current investigation show small dimensions in thickness, i.e. ∼3–10 nm, in lower bainite. An ε carbide $Fe_{2.4}C$ particle with a thickness of ∼10 nm and a cementite particle with a thickness of ∼5 nm are indicated in Fig. 3a. From Fig. 3, these nanosized precipitates are inferred to form under paraequilibrium mode. Likewise, the same stoichiometry of ε carbide $Fe_{2.4}C$ and the same elemental partitioning behavior of interstitial and substitutional elements across the bainitic ferrite α_B/ε carbide $Fe_{2.4}C$ interface are revealed in Fig. 4. The ε carbide $Fe_{2.4}C$ particle indicated in Fig. 4 shows a thickness of ∼4 nm. Small regions of carbon agglomeration in the bainitic ferrite α_B matrix are again detected in this dataset (Fig. 4a). ε carbide $Fe_{2.4}C$ precipitation in lower bainite is repeatedly proved to occur under paraequilibrium mode.

These results help us to gain further knowledge of the shapes of cementite (θ) and ε carbide $Fe_{2.4}C$ in lower bainite in three dimensions together with the chemical composition and the local partitioning behavior. The TEM observations also show these nanocarbides in the lower bainite, however, only in the form of 2-D projections, as indicated in Fig. 2a. The TEM results also suggest that the nanocarbides in the current lower bainite assume elongated shapes with an average size of ∼30 nm in width and ∼80 nm in length. On the other hand, in our APT measurements we detected additional nanocarbides in lower bainite even with a much smaller size of ∼3–10 nm in thickness. When compared to the average width and length values of the nanosized carbides in the lower bainite observed by TEM, we find that the thicknesses of these carbides that are revealed by APT are much smaller. Therefore, when blending the TEM observations on the average width and length of the nanosized carbides in the lower bainite with the current APT results, we conclude that both cementite (θ) and ε carbide $Fe_{2.4}C$ adopt plate-like carbide shapes.

The 3-D carbon atom map of the sample isothermally heat-treated at 500 °C for 1200 s is shown in Fig. 5a. Fig. 5a shows a local overview of the carbon distribution in bainitic ferrite α_B and cementite (θ) in upper bainite in 100Cr6. The carbon-rich region with a carbon content of ∼25 at.% corresponds to cementite (θ). The carbon-depleted region in the bulk represents bainitic ferrite α_B. The carbon content in the α_B bulk phase amounts to only ∼0.0173 at.%. The carbon largely partitions to the austenite during upper bainite formation at 500 °C, which leads to carbide precipitation directly from austenite.

Fig. 5b displays the proxigram of carbon and alloying elements at the interface of bainitic ferrite α_B and cementite (θ) in upper bainite. The proxigram reveals the partitioning characteristics of carbon and alloying elements at the bainitic ferrite (α_B)/cementite (θ) interface. As shown in Fig. 5b, the carbon partitions according to the local equilibrium between bainitic ferrite (α_B) and cementite (θ), while the substitutional elements Cr, Mn and Si redistribute over a short range and exhibit enrichment at the α_B/θ interface. Si is mostly dissolved in the bainitic ferrite matrix and exhibits a relatively low solubility in cementite (θ). Fig. 5b shows that Si is highly enriched at the interface between the bainite and the cementite (θ), which kinetically impedes the further growth of cementite (θ). However, the data also reveal that there is no long range redistribution of the substitutional elements Cr, Mn and Si.

It is assumed in the paraequilibrium mode that only interstitial elements are considered to be equilibrated, while in the non-partitioning local equilibrium/negligible partitioning local equilibrium (NPLE) mode, interstitial

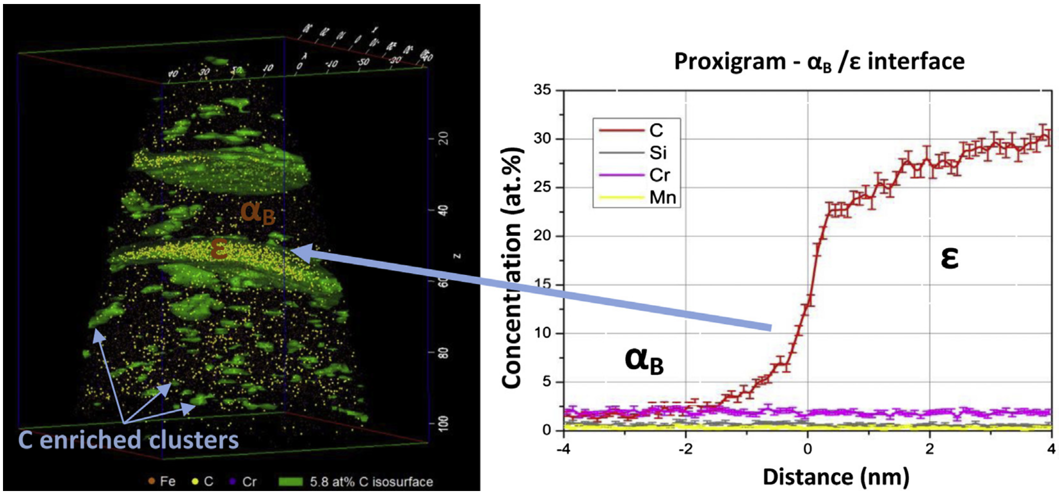

Fig. 4. (a) 3-Dimensional atomic map and 5.8 at.%C iso-concentration surface in lower bainite in 100Cr6 isothermally heat-treated at 260 °C for 2500 s; (b) proxigram showing carbon and alloy concentrations across bainitic ferrite and ε carbide $Fe_{2.4}C$ interface; α_B: bainitic ferrite, ε: ε carbide $Fe_{2.4}C$.

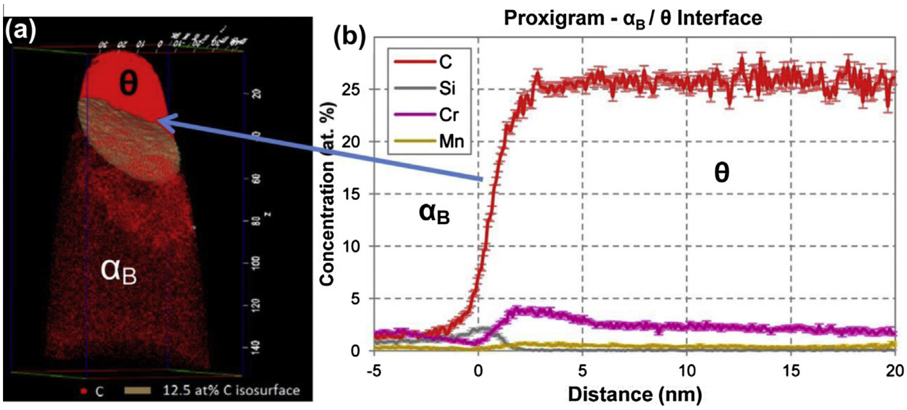

Fig. 5. (a) Carbon atomic map and 12.5 at.% iso-concentration surface in upper bainite in 100Cr6 isothermally heat-treated at 500 °C for 1200 s; (b) proxigram showing carbon and alloy concentrations across bainitic ferrite and cementite (θ) interface; α_B: bainitic ferrite, θ: cementite.

elements partition according to the local equilibrium and substitutional elements redistribute over a short range. The various interstitial and substitutional elemental partitioning features in the current APT investigation indicate that cementite (θ) and ε carbide $Fe_{2.4}C$ precipitate under paraequilibrium mode in lower bainite at 260 °C, while cementite (θ) precipitates under NPLE mode in upper bainite at 500 °C.

Unlike the nanosized carbides in lower bainite, the cementite (θ) that precipitated in the upper bainite exhibits a much larger average size. The coarsened carbides even achieve a size of up to 1 μm in length. Thus, APT maps are not capable of revealing the complete size information of a coarse cementite (θ) in upper bainite.

4.3. Ab initio calculations

Ab initio calculations were performed in order to assess the thermodynamic probability of ε carbide $Fe_{2.4}C$ formation, competing with the precipitation of cementite (Fe_3C, θ). As the most crucial prerequisite for total-energy calculations, a reliable structural model for ε carbide is needed, in particular because the distribution of the n carbon atoms over the $2.4n$ available octahedral sites is not fully resolved. For the structure of the hexagonal ε-Fe_3C, on the other hand, the situation is clear ever since its first synthesis in 1950 [46]. For illustration, Fig. 6a depicts the commonly used unit cell of the hexagonal Fe carbide structures containing six Fe atoms. For carbon, three different independent crystallographic positions, called Wyckoff sites, are available (2*b*, 2*c*, 2*d*). Each site corresponds to two indistinguishable atomic positions which can be occupied by C atoms. In ε-Fe_3C (Fig. 6(b)), only the 2*d* position is fully occupied, thereby leading to the widest possible C–C distances ($d = 3.49$ Å) and corner-sharing octahedra throughout.

For this work, the question of carbon ordering is of paramount importance. Indeed, the aforementioned ordering proposed by Jack [18] for $Fe_{2.2}C$ was corroborated by several DFT total-energy calculations for ε-Fe_2C [47–49] and also ε-$Fe_{2.4}C$ [4]. In a recent experimental contribution, Du Plessis synthesized a mixture of iron carbides with ε-$Fe_{2.3}C$ (the carbon content is somewhat sample dependent [22]) being the main phase [23]. Rietveld refinement of X-ray data, however, did not show any indications for carbon ordering but suggested that the disordered [NiAs] structure type (with space group $P6_3/mmc$; *Strukturbericht* Designation: $B8_1$) is more likely, thereby questioning the theory. In other words, the C atoms would then randomly occupy 41.7% of each of the Wyckoff positions 2*b*, 2*c* and 2*d* (Fig. 6d). Therefore we first clarified the situation by independent theoretical means. In the most common description of the ordered variant of Fe_2C (note that the only published structure of Fe_2C in the ICSD database [50] is obviously incorrect) the C atoms occupy all the 2*d* sites such as in Fe_3C and, additionally, a single position, or 50%, of the 2*b* sites (see Fig. 6c). This leads, next to the corner-sharing octahedra described above, to additional edge-sharing octahedra with a C–C distance of 2.73 Å. Nonetheless, face-sharing octahedra with a C–C distance of 2.17 Å do not occur in the ordered variant because carbon does not occupy the 2*c* sites. According to Pauling's third rule of crystal chemistry, the latter polyhedral connectivity is energetically unfavorable [51]. Our density-functional comparison of both candidates confirms Pauling's rule because the calculation of the ordered distribution of ε-Fe_2C indicates this to be 41 kJ mol^{-1} more stable at 0 K than the disordered one; this is an extremely large difference between two different interstitial configurations. For the same reason, the phase dubbed $Fe_{2.4}C$ would also have the 2*d* sites completely occupied by carbon and the 2*b* site only partially occupied (25%). If we compare this structure with a disordered ε-$Fe_{2.4}C$, the energy gain amounts to 39 kJ mol^{-1} at 0 K (Fig. 7). At higher temperatures the energetic difference of the disordered structure gets slightly reduced since it is stabilized by the configuration entropy term. The latter term, however, will never compensate this large enthalpy difference up to the melting point. Therefore, the existence of a disordered ε-$Fe_{2.4}C$ can be safely excluded at any temperature.

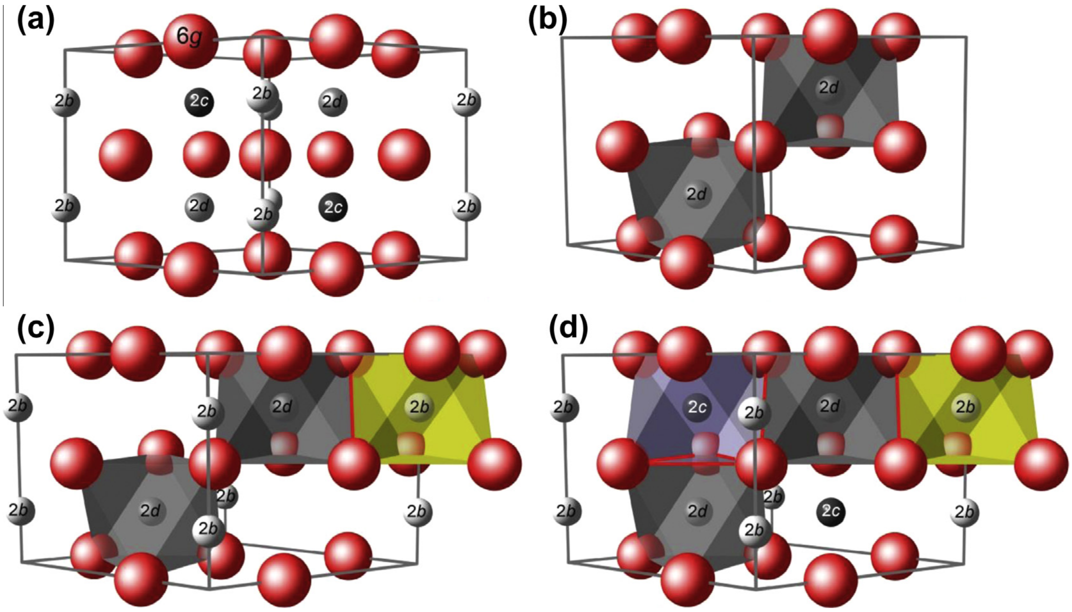

Fig. 6. Hexagonal close-packed unit cell of Fe (in red) containing all possible octahedral Wyckoff sites 2*b* (white), 2*c* (black), and 2*d* (grey) for the carbon atoms (a); the ordered ε-Fe_3C has only carbon-filled corner-sharing octahedra (grey) by occupying all 2*d* sites (b). In the ordered variant of the carbon-richer $Fe_{2.4}C$, edge-sharing octahedra (red line between grey and yellow octahedra) also occur by filling 25% of the 2*b* site (c) while in disordered $Fe_{2.4}C$ they would also be face-sharing (common plane between blue and grey octahedra; tagged with a red triangle) since Wyckoff site 2*c* is partially occupied. Red lines emphasize common edges and faces (in d) between adjacent octahedra. The Wyckoff positions have been indicated.

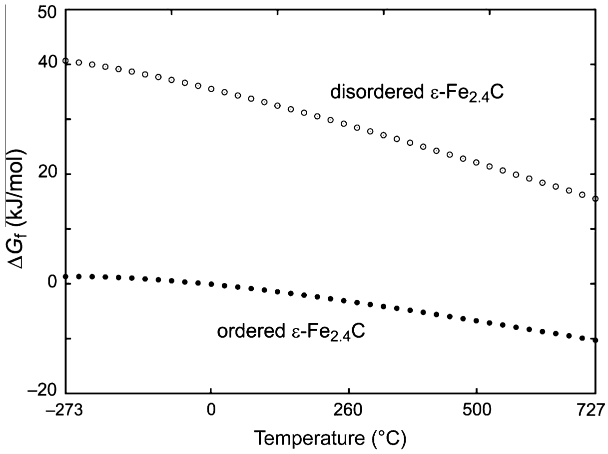

Fig. 7. Comparison of stabilities (Gibbs free energies of formation) of randomly occupied and ordered ε carbide $Fe_{2.4}C$ as a function of temperature.

Since cementite (θ) and ε-$Fe_{2.4}C$ have different stoichiometries, a direct comparison of their enthalpies is not possible such that we have to generate a realistic thermodynamic balance between both phases in order to compare the competing products. The obvious reaction in an iron matrix is the transition between ε carbide/iron and cementite (θ):

$$\varepsilon\text{-}Fe_{2.4}C + 0.6\ Fe \rightleftarrows \theta\text{-}Fe_3C$$

where Fe is either body-centered cubic (bcc) iron in a bainitic–ferritic matrix at low temperatures or face-centered cubic (fcc) iron in austenite at higher temperatures. We calculated the Gibbs free energies for the aforementioned reaction as a function of temperature and the results are shown in Fig. 8. A positive value of the Gibbs free energy indicates an ε favored region and a negative value indicates a cementite favored regime. In a bainitic ferrite matrix and at 0 K, the Gibbs free energy of the reaction is $-1.5\ \text{kJ mol}^{-1}$ which means that the formation of cementite (θ) is slightly more favorable than the formation of the hexagonal carbide. Upon increasing the temperature, however, the reaction becomes more equilibrated ($\Delta G_R \approx 0$) because the slightly higher configurational entropy contribution (due to more degrees of freedom because of partial carbon disorder) of the ε carbide reduces this energy difference. At 260 °C, the Gibbs energy is $\sim 0.1\ \text{kJ mol}^{-1}$ only and the formation of θ-Fe_3C and ε-$Fe_{2.4}C$ have nearly the same probability from a thermodynamic standpoint. In an austenitic environment, however, the formation of cementite (θ) is clearly preferred at any temperature; for example, at 500 °C it is favored by $4\ \text{kJ mol}^{-1}$. The theoretical results reveal that the formation of epsilon carbide does not directly depend on the temperature because cementite is even more favored at low temperatures. Indirectly, however, it does depend on the temperature since the formation benefits from a ferritic matrix. As carbides precipitate exclusively from austenitic matrix in upper bainite, it is inferred in terms of thermodynamics that only cementite (θ) can precipitate at 500 °C in upper bainite, while both cementite (θ) and ε-$Fe_{2.4}C$ precipitation can occur at 260 °C in lower bainite. Furthermore, ε carbide is more prone to precipitate from lower bainite than from upper bainite.

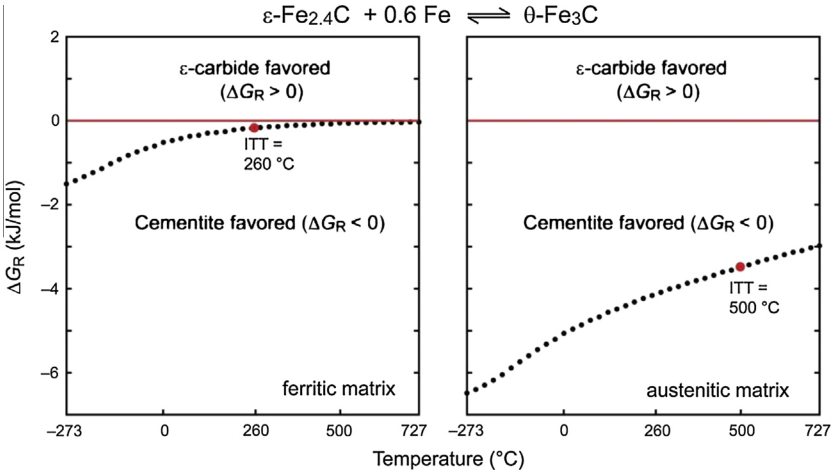

Fig. 8. Gibbs free reaction energies between ε-$Fe_{2.4}C$ and cementite (Fe_3C, θ) as a function of temperature in a ferritic (left) and an austenitic matrix (right). Both experimental isothermal transformation temperatures (ITT) are indicated.

5. Conclusions and outlook

ε and θ carbide precipitation and elemental partitioning behavior in both upper and lower bainite were investigated in high-carbon bearing steel 100Cr6 using TEM and APT in combination with ab initio (density-functional theory) calculations. The long-lasting questioning of ε carbide existence and its transition to θ carbide is proved in terms of elemental concentrations detected by APT and explained by thermodynamic simulations. The nanosized metastable carbides precipitate from upper bainite and from lower bainite under different mechanisms. The difference of the two precipitation mechanisms within bainite is revealed for the first time by means of atomic-scale investigation on the elemental partitioning behaviors. Deeper insights into the nature of ε and θ carbide precipitation were gained at the atomic scale. In the future, in order to prove our APT observations in a crystallographic manner and to further explore the metastable carbide precipitation within bainite structure as well as the ε → θ transition during bainitic phase transformation, time-resolved in situ high-energy synchrotron X-ray and TEM analysis will be carried out. In the present work, the results can be summarized as follows:

1. APT measurements show that both ε and θ precipitate in lower bainite isothermally held at 260 °C and only θ precipitates in upper bainite isothermally held at 500 °C.
2. TEM and APT reveal different sizes of ε and θ carbides at 260 and 500 °C. Both, ε and θ carbides adopt plate-like shapes in lower bainite.
3. APT reveals that ε and θ precipitate under paraequilibrium mode at 260 °C in lower bainite, and θ precipitates under NPLE mode in upper bainite at 500 °C.
4. In lower bainite formation at 260 °C, a high amount carbon trapping within bcc leads to carbide precipitation from bainitic ferrite. In upper bainite formation at 500 °C, sufficient carbon partitioning to fcc leads to carbide precipitation from austenite.
5. Ab initio calculations reveal that the ε carbide must be a partially ordered structure with respect to the carbon distribution.
6. From a thermodynamic point of view, the probability of forming cementite and ε carbide in a bainitic ferrite matrix is comparable. In austenite, however, the formation of cementite is clearly preferred, namely favored by 5 kJ mol^{-1} at room temperature and still by 4 kJ mol^{-1} at 500 °C. This indicates that ε carbide is more prone to precipitation from lower bainite than from upper bainite.

Acknowledgements

This work has been performed partly within the Interdisciplinary Centre for Advanced Materials Simulation (ICAMS) at Ruhr University Bochum and partly within the collaborative research center (SFB) 761 of the Deutsche Forschungsgemeinschaft at RWTH Aachen University. The authors would like to express their thanks to Dr. Christoph Somsen in Ruhr-University Bochum for his support with the TEM experiment and the Center for High Performance Computing of RWTH Aachen University for providing us with computational time for the ab initio investigations. ICAMS gratefully acknowledges funding from ThyssenKrupp Steel Europe AG, Bayer Material Science AG, Salzgitter Mannesmann Forschung GmbH, Robert Bosch GmbH, Benteler Steel/tube Management GmbH, Bayer Technology Services GmbH and the state of North Rhine-Westphalia as well as the European Commission in the framework of the European Regional Development Fund (ERDF).

References

[1] Barrow ATW, Kang JH, Rivera-Daz-del-Castillo PEJ. Acta Mater 2012;60:2805.

[2] Kang JH, Hosseinkhani B, Rivera-Daz-del-Castillo PEJ. Mater Sci Technol 2012;28:44.

[3] Jang JH, Kim IG, Bhadeshia HKDH. Scripta Mater 2010;63:121.

[4] Fang CM, van Huis MA, Zandbergen HW. Scripta Mater 2010;63:418.

[5] Zhu C, Cerezo A, Smith GDW. Ultramicroscopy 2009;109:545.

[6] Kim IG, Rahman G, Jang JH, Song YY, Seo SW, Bhadeshia HKDH, et al. Mater Sci Forum 2010;47:654.

[7] Amulevicius A, Mazeika K, Daugvila A. J Phys D: Appl Phys 2000;33:1985.

[8] Waterschoot T, Verbeken K, De Cooman BC. ISIJ Int 2006;46:138.

[9] Bała P, Pacyna J. J Achieve Mater Manuf Eng 2007;23:15.

[10] Casteletti LC, Riofano RMM, Nascente PAP. Mater Sci Technol 2004;20:1171.

[11] Perez M, Sidoroff C, Vincent A, Esnouf C. Acta Mater 2009;57:3170.

[12] Tarlor KA, Olson GB, Cohen M, vander Sande JB. Metall Trans A 1988;20A:2749.

[13] Brown JE, Smith GDW. Surf Sci 1991;246:285.

[14] Zhu C, Xiong XY, Cerezo A, Hardwicke R, Krauss G, Smith GDW. Ultramicroscopy 2007;107:808.

[15] Lai GY. Metall Trans A 1975;6A:1469.

[16] Caballero FG, Miller MK, Garcia-Mateo C. Metall Mater Trans A 2011;42A:3660.

[17] Hofer LJE, Cohn EM, Peebles WC. J Am Chem Soc 1949;71:189.

[18] Jack KH. J Iron Steel Inst 1951;169:26.

[19] Johnston WD, Heikes RR, Petrolo J. J Phys Chem 1960;64:1720.

[20] Ruixue W, Baoshan W, Yongwang L. Chin J Catal 2012;33:863.

[21] Niemantsverdriet JW, van der Kraan AM, van Dijk WL, van der Baan HS. J Phys Chem 1980;84:3363.

[22] Dirand M, Afqir L. Acta Metall 1983;31:1089.

[23] Du Plessis HE. PhD thesis, University of Johannesburg; 2008.

[24] Miller MK. Atom probe tomography: analysis at the atomic level. New York: Kluwer Academic/Plenum Press; 2000.

[25] Seol JB, Raabe D, Choi P, Im YR, Park CG. Acta Mater 2012;60:6183.

[26] Dmitrieva O, Ponge D, Inden G, Millán J, Choi P, Sietsma J, et al. Acta Mater 2011;59:364.

[27] Marquis EA, Choi P, Danoix F, Kruska K, Lozano-Perez S, Ponge D, et al. Microsc Today 2012;20:44.

[28] Caballero FG, Miller MK, Babu SS, Garcia-Mateo C. Acta Mater 2007;55:381.

[29] Hohenberg P, Kohn W. Phys Rev 1964;136:864.

[30] Kohn W, Sham LJ. Phys Rev 1965;140:1133.

[31] Blöchl PE. Phys Rev B 1994;50:17953.

[32] Kresse G, Hafner J. J Phys Condens Matter 1994;6:8245.

[33] Kresse G, Furthmüller. J Comput Mater Sci 1996;6:15.

[34] Kresse G, Furthmüller. J Phys Rev B 1996;54:11169.

[35] Parlinski K, Li ZQ, Kawazoe Y. Phys Rev Lett 1997;78:4063.

[36] Togo A. Fropho: a tool to compute phonon band structures and thermal properties of solids. RWTH Aachen University; 2008.

[37] Togo A, Oba F, Tanaka I. Phys Rev B 2008;78:134106.

[38] Hellmann H. Einführung in die Quantenchemie. Leipzig, Wien: Franz Deuticke; 1937.

[39] Feynman RP. Phys Rev 1939;56:340.

[40] Dove MT. Introduction to lattice dynamics. Cambridge: Cambridge University Press; 1993.

[41] Stoffel RP, Wessel C, Lumey MW, Dronskowski R. Angew Chem Int Ed 2010;49:5242.

[42] Li YJ, Choi P, Borchers C, Westerkamp S, Goto S, Raabe D, et al. Acta Mater 2011;59:3965.

[43] Li YJ, Choi P, Goto S, Borchers C, Raabe D, Kirchheim R. Acta Mater 2012;60:4005.

[44] Matsuda H, Bhadeshia HKDH. Proc Roy Soc Lond A 2004;460:1707.

[45] Hillert M, Höglund L, Ägren J. Acta Metall Mater 1993;41:1951.

[46] Jack KH. Acta Cryst 1950;3:392.

[47] Shang SL, Böttger AJ, Liu ZK. Acta Mater 2008;56:719.

[48] Fang M, van Huis MA, Jansen J, Zandbergen HW. Phys Rev B 2011;84:094102.

[49] Fang CM, van Huis MA, Zandbergen HW. Scripta Mater 2011;64:296.

[50] Inorganic Crystal Structure Database, National Institute of Standards and Technology (NIST) and Fachinformationszentrum Karlsruhe, #162103; 2009.

[51] Pauling L. The nature of the chemical bond. 3rd ed. Ithaca, NY: Cornell University Press; 1960.